

## Low-temperature magnetoelectroluminescence of organic light-emitting diodes: Separating excitonic effects from carrier-pair singlet-triplet mixing

F. Braun<sup>1</sup>, T. Scharff<sup>1</sup>, S. Bange<sup>1</sup>, W. Jiang<sup>2</sup>, T. A. Darwish<sup>3,4</sup>, P. L. Burn<sup>2</sup>, V. V. Mkhitarian<sup>1,\*</sup> and J. M. Lupton<sup>1</sup>

<sup>1</sup>*Institut für Experimentelle und Angewandte Physik, Universität Regensburg, Universitätsstraße 31, 93053 Regensburg, Germany*

<sup>2</sup>*Centre for Organic Photonics & Electronics, School of Chemistry and Molecular Biosciences,*

*The University of Queensland, Brisbane, Queensland 4072, Australia*

<sup>3</sup>*National Deuteration Facility, Australian Nuclear Science and Technology Organization (ANSTO), Lucas Heights, New South Wales 2234, Australia*

<sup>4</sup>*Faculty of Science and Technology, University of Canberra, Australian Capital Territory 2617, Australia*



(Received 17 March 2024; revised 27 May 2024; accepted 4 June 2024; published 17 July 2024)

Low-temperature magnetoelectroluminescence (MEL) of organic light-emitting diodes (OLEDs) reveals a near-complete suppression of electroluminescence at strong magnetic fields due to the high degree of thermal spin polarization (TSP) arising when the Zeeman energy exceeds the thermal energy. In addition to TSP, spin mixing within the Coulombically bound carrier pairs can arise, as can interactions between triplet excitons or triplet excitons and charge carriers. These effects also depend on the applied magnetic field strength. We report on the surprisingly nonmonotonic MEL in the intermediate magnetic-field region of up to 230 mT at temperatures down to 1.5 K, and explore the effect of deuteration to distinguish between triplet-excitonic and carrier-pair effects. A narrow MEL feature is observed in the field region of  $\pm 3$  mT, which is inverted upon deuteration and can therefore be clearly assigned to spin mixing mediated by the hyperfine fields. At larger fields, a broader MEL feature is identified, which shows discrete substructure assigned to the zero-field splitting of the triplet exciton. The resolution of this substructure is enhanced by deuteration. Quantitative modeling of the MEL by solving the stochastic Liouville equation in the density-matrix formalism provides excellent agreement with the experimental results and demonstrates that the triplet excitonic feature arises from delayed fluorescence generated by triplet-triplet annihilation (TTA). The microscopic simulations reveal that TTA occurs preferentially when the axes of the two triplets in the amorphous  $\pi$ -conjugated polymer are close to parallel to each other, illustrating an alternative spectroscopic approach to investigating the underlying physics of TTA.

DOI: [10.1103/PhysRevB.110.014204](https://doi.org/10.1103/PhysRevB.110.014204)

### I. INTRODUCTION

Organic light-emitting diodes (OLEDs) exhibit a range of intriguing magnetic-field effects, both in magnetoresistance (MR) and magnetoelectroluminescence (MEL), offering an experimental platform to provide insight into fundamental aspects of electronic spin physics. An electron or hole spin of an organic semiconductor in a magnetic field constitutes a near-perfect two-level system. Under magnetic-resonant drive, for example, Floquet states can form that give rise to unusual multiphoton transitions [1]. The interaction between electron and hole spins is governed by the nuclear hyperfine fields of the active material in the OLED, which can be controlled by deuteration of the emissive material. This hyperfine interaction gives rise to extraordinary sensitivity of both MR and MEL, allowing magnetic fields to be detected down to the level of a few hundred nanoteslas, merely a percent of geomagnetic field strengths [2]. On top of this, when the molecules in an organic semiconductor film are in an anisotropic arrangement, substantially anisotropic MR and MEL can occur. For example, at geomagnetic field strengths,

simple polymer OLEDs can show anisotropic MR of 35%, conceivably providing a solid-state analogy to the radical-pair processes [3] that have been invoked to rationalize biological magnetoreception phenomena [4].

In an OLED, electrons and holes are injected electrically. Coulombic interactions lead to the formation of weakly spin-spin and exchange-coupled carrier pairs, often referred to as polaron pairs (PPs), which exist in singlet or triplet permutation symmetry. These PPs can ultimately recombine to form molecular excitons, also of singlet or triplet character, whereby in most hydrocarbon materials (i.e., those not containing heavy atoms that give rise to substantial spin-orbit coupling and mixing of singlet and triplet states), only the singlet species are emissive. There are five principal ways in which a magnetic field can influence the operation of an OLED. (1) The so-called PP recombination mechanism [5–7] is governed by the spin precession in local hyperfine fields, which serves to mix singlet and triplet PPs. A weak to intermediate external magnetic field will modify spin precession, ultimately quenching it and suppressing singlet-triplet spin mixing. (2) A second source of spin mixing arises from weak but finite spin-orbit coupling, which gives rise to a distribution of effective electronic  $g$  factors. In this “ $\Delta g$  effect,” slight differences in Larmor frequencies of the constituent spins of

\*Contact author: [vagharsh.mkhitarian@ur.de](mailto:vagharsh.mkhitarian@ur.de)

the PP exist, which become more pronounced with increasing external magnetic-field strength [6,7]. (3) In addition, at very low temperatures and very high fields, the Zeeman splitting of the individual carrier spins becomes comparable to the thermal energy. In this case, thermal spin polarization (TSP) of the carrier spins can arise, quenching singlet PP formation and ultimately leading to a pure triplet excitonic population [8,9]. Because triplet excitons have a spin of  $S = 1$  they can also be the source of magnetic-field effects, either (4) through the interaction with individual polarons (the triplet-exciton polaron interaction, TPI) or (5) through triplet-triplet annihilation (TTA), which leads to delayed fluorescence [5,6,10–12]. Even when triplets are nonemissive, signatures of TPI can be observable in the MEL measurement through a spin-allowed triplet-to-singlet up-conversion process [12–14].

We recently reported a detailed study of TSP in OLEDs, demonstrating near-unity spin polarization and the resulting suppression of electroluminescence (EL) at low temperatures and high fields [8]. However, TSP was found to depend strongly on the current density in the device, and a perfect Boltzmann-type dependence could only be observed for extremely low currents of 550 nA, barely above the detection threshold of the EL. For larger currents, the MEL functional dependence appeared nonmonotonic at very low fields and exhibited a smaller dynamic range. Here, we investigate these MEL measurements at low temperatures ( $\sim 1.5$  K) in the intermediate magnetic-field range of  $\pm 230$  mT, with the aim of distinguishing between pure hyperfine-mediated spin-pair effects from phenomena relating to triplet excitons. To identify the hyperfine effects conclusively, we compare a conventional protonated conjugated polymer to an analogous perdeuterated material [15]. To determine the possible influence of triplet excitons in the MEL, we search for signatures of the substructure of the triplet excitons, the zero-field splitting (ZFS), which is known from magnetic resonance spectroscopy [16]. Calculations based on solving the stochastic Liouville equation in the density-matrix formalism provide excellent agreement with the experimental observations, allowing us to distinguish between the different mechanisms.

## II. EXPERIMENTAL METHODS

The OLED structure and its fabrication process are identical to that reported in our previous study [3], with only a difference in the encapsulation method that allowed the sample to be inserted into the cryostat and cooled down to 1.5 K. Encapsulation was achieved by thermal evaporation of a 500-nm-thick layer of  $N,N'$ -bis(3-methylphenyl)- $N,N'$ -diphenylbenzidine (TPD) prior to removing the device from the glovebox. The cryostat (American Magnetics) is comprised of a split-coil superconducting magnet, a variable temperature insert (VTI), and windows for optical access. The OLED drive currents were chosen such that no discernible warming of the OLED occurred within the bath cryostat [8]. The OLED EL was imaged onto a scientific complementary metal-oxide semiconductor camera (Hamamatsu), placed roughly 0.7 m away from the magnet, using a lens system. All OLEDs were operated in constant-current mode, using a low-noise source-measure unit (Keithley 2400), which also recorded the device voltage. Magnetic field sweeps

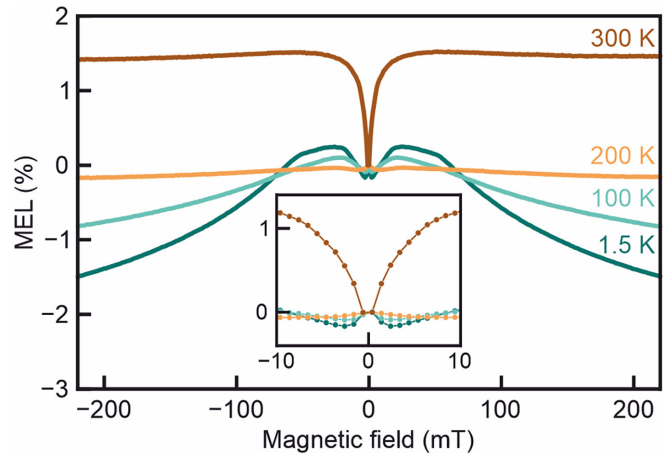


FIG. 1. Temperature dependence of the MEL of a h-MEH-PPV OLED, at a constant current of 100  $\mu$ A. The inset shows a close-up of the low field region.

with the field direction perpendicular to the device surface were performed from  $-230$  to  $230$  mT, repeated 20 times for the low-resolution measurements and 4 times for the high-resolution measurements with a much longer measurement time. For the high-resolution measurements, the current through the magnet was controlled by a proportional-integral-derivative (PID) controller using a current precision of 0.1 mA, which translates to a magnetic field of 11  $\mu$ T in the superconducting magnet. The regular spacing between magnetic field points in the low-resolution sweeps was 1 mT. For some measurements, the spacing between the field points was decreased to 110  $\mu$ T between  $-11$  and  $11$  mT. Since the measurement time for these high-resolution sweeps is significantly longer, they were only used to ensure that the lower-resolution measurements did not introduce artifacts in the reference to zero field. The measured EL intensity is then used to calculate the MEL, which is defined as  $EL(B)/EL(0) - 1$ . For experimental reasons, in order to reach the lowest temperatures, this study used a superconducting magnet for all experiments. Note that this is an unconventional choice given the precision requirements for magnetic fields necessary for high-resolution MEL around the origin. Details of the measurement procedure are discussed in Sec. V C.

## III. EXPERIMENTAL RESULTS

### A. Temperature dependence of MEL

Figure 1 presents temperature-dependent MEL measured for an OLED composed of an emissive layer of the regular protonated poly[2-methoxy-5-(2'-ethylhexyloxy)-1,4-phenylene vinylene] (h-MEH-PPV). Remarkably, the MEL changes its sign, from essentially negative at low temperatures to positive at room temperature. In the low-field region around  $\pm 10$  mT, the sign change is more convoluted, with an initial drop occurring at 1.5 K turning into a steep rise at room temperature. Such a steep field dependence is characteristic of spin-conserving PP recombination (PPR) [6,7,17,18], in which, besides the external magnetic field, spins are subject to local hyperfine fields of typically  $\lesssim 1$  mT. This observation is further supported by the fact that the PPR mechanism can

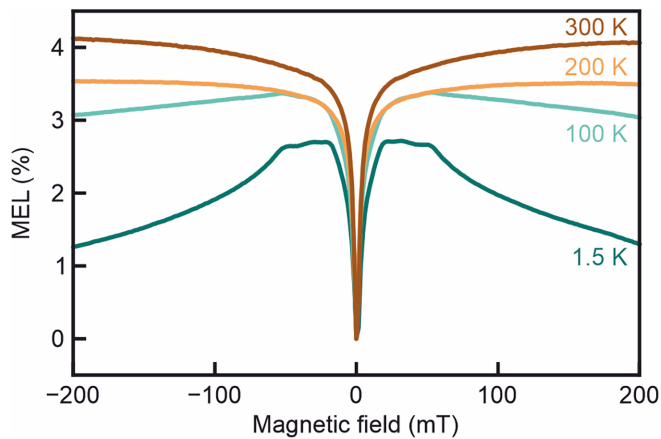


FIG. 2. Temperature dependence of the MEL of a d-MEH-PPV OLED, at a constant current of 100  $\mu\text{A}$ .

lead to either positive or negative MEL, depending on the relative magnitudes of the singlet and triplet exciton formation rates [19], and the sign change may occur because of the temperature dependence of PP formation rates as discussed below.

A direct way to scrutinize the presumably hyperfine-controlled low-field behavior of MEL is to explore similar OLED structures with an emissive layer possessing a different hyperfine interaction strength. This motivated our investigation of devices comprising a perdeuterated conjugated polymer, d-MEH-PPV, in which the hyperfine coupling is known to be weaker by a factor of  $\sim 3$  [15,17].

### B. Effect of deuteration on low-temperature MEL

In Fig. 2, the MEL of a d-MEH-PPV device is shown. In this case, there is no sign change with the temperature, and the MEL is always positive. However, the low-field behavior of the MEL in Fig. 2 is even steeper than that of the MEL of the h-MEH-PPV device. This observation is in direct support of PPR being the underlying mechanism of the low-field component of MEL: the weaker the hyperfine fields, the steeper the MEL in the low-field regime [6,18,20].

Besides the low-field component, the MEL responses in Figs. 1 and 2 show a broad shoulder structure at around  $\pm 50$  mT at low temperatures that disappears at higher temperatures. Given the magnetic-field scale, we tentatively attribute this structure to spin-dependent reactions involving triplet excitons. Magnetic-resonance spectroscopy of h-MEH-PPV has revealed a triplet sublevel splitting of the order of 50 mT [16]. With increasing temperature, the shoulder structure fades away, presumably because of the reduction of the triplet exciton lifetime [21]. In the following, we identify the spin-dependent process involving the triplet exciton as triplet-triplet annihilation (TTA).

To recap the two preceding sections, from Figs. 1 and 2 we infer that the low-temperature MEL is dominated by the PPR mechanism in the low-field region around  $|B| \lesssim 10$  mT and by the TTA mechanism outside of this low-field region, at fields of up to  $|B| \leq 230$  mT. With increasing temperature, however, the TTA component disappears because of the depletion of triplet population by the reduction in triplet

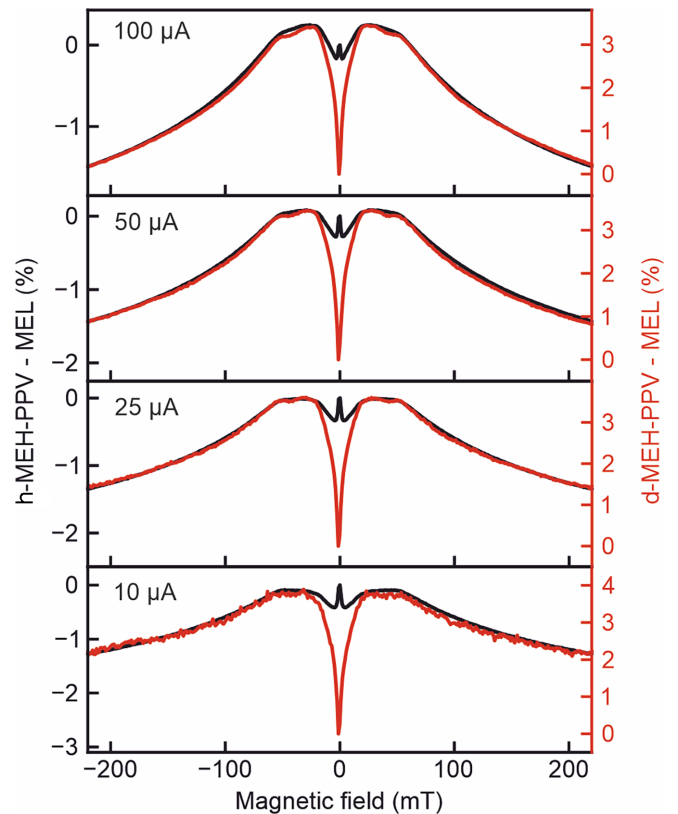


FIG. 3. Current dependence of the MEL, measured for devices with h-MEH-PPV and d-MEH-PPV emissive layers, at 1.5 K.

lifetime, and the MEL becomes entirely PPR controlled. Remarkably, the PPR-induced MEL changes its sign with changing temperature for h-MEH-PPV devices, going from negative to positive, whereas it is always positive for d-MEH-PPV at all temperatures probed.

### C. Current dependence of MEL

In Fig. 3, the current-dependent MEL of two OLEDs comprising either protonated or perdeuterated MEH-PPV are superimposed, showing their strongly contrasting field dependence at low fields and the overall similarity at intermediate to higher fields. The figure reinforces the breakdown of basic processes underlying the MEL to polaron-pair-related (and hence hyperfine-field-controlled) and triplet-exciton-related components and reveals the congruity of these processes in the two devices. The main difference between the MEL in the two devices is the sign of the amplitude of the low-field components, which is positive for the deuterated polymer and negative for the protonated version. The following theoretical analysis confirms this qualitative picture and provides a quantitative assessment of the MEL.

## IV. THEORY

OLED operation is based on the injection of charge carriers, with the subsequent formation of excitons. For the triplet

and singlet exciton densities,  $T$  and  $S$ , we utilize the rate equations [22]

$$\frac{dT}{dt} = G_T - \frac{T}{\tau_T} - \Gamma T^2, \quad (1)$$

$$\frac{dS}{dt} = G_S - \frac{S}{\tau_S} + \Phi T^2, \quad (2)$$

where  $G_T$  and  $G_S$  are the triplet and singlet exciton generation rates,  $\tau_T$  and  $\tau_S$  are the triplet and singlet lifetimes,  $\Gamma$  is a bimolecular triplet-triplet interaction rate, and the last term describes the fusion of two triplets to a singlet via TTA with the rate  $\Phi$ . Thus,  $\Phi/\Gamma$  determines the probability that TTA results in the creation of an emissive singlet. The above description neglects direct and reverse inter-system crossing processes, singlet-singlet and singlet-triplet quenching, and other higher-order processes, which we do not find to be relevant in modeling the operation of these OLEDs.

The device MEL is proportional to  $S$ , under steady-state conditions in an externally applied magnetic field  $B$ . Under such conditions, implying time-independent  $S$  and  $T$ , the solution of Eqs. (1) and (2) for the singlet density is found to be

$$\bar{S} = \tau_S G_S + \frac{4\Phi\tau_S(\tau_T G_T)^2}{(1 + \sqrt{1 + 4\Gamma\tau_T^2 G_T})^2}. \quad (3)$$

In the subsequent discussion, bars over the different quantities denote their steady-state values. Two limiting regimes controlled by the relative strength of the lifetime and the bimolecular triplet-triplet interaction terms in Eq. (1) can be distinguished. These two terms scale as  $\propto\tau_T^{-1}$  and  $\propto\Gamma\tau_T G_T$ , respectively, so their relative strength is given by the parameter  $\xi = \Gamma\tau_T^2 G_T$ , with a larger  $\xi$  implying stronger triplet-triplet interaction. In the two extreme regimes of  $\xi$ , the limiting values are

$$\begin{aligned} \bar{S} &\cong \tau_S G_S + \Phi\tau_S\tau_T^2 G_T^2, & \xi \ll 1, \\ \bar{S} &\cong \tau_S G_S + (\Phi/\Gamma)\tau_S G_T, & \xi \gg 1. \end{aligned} \quad (4)$$

The magnetic-field dependence in Eqs. (3) and (4) comes from the  $B$  dependence of the rates,  $G_S(B)$ ,  $G_T(B)$ ,  $\Gamma(B)$ ,  $\Phi(B)$ , and that of the triplet lifetime,  $\tau_T(B)$ . To specify these  $B$  dependencies, microscopic models of PPR, TTA, and TPI are considered in the following.

### A. The polaron-pair recombination (PPR) model

Generation of excitons from the injected electrons and holes is mediated by the formation of weakly spin-spin and exchange-coupled electron-hole (polaron) pairs [5–7]. Depending on the total spin of the constituent carriers, the PPs combine into singlet or triplet excitons as this process is spin conserving. Because the spins in a pair are subject to internal and external magnetic fields, the total spin of the pair is dynamic and field dependent. Hence, the generation rates,  $G_S$  and  $G_T$ , are  $B$  dependent and this dependence is governed by the spin multiplicity dynamics in the ensemble of PPs.

The quantitative description of this process is given by the PPR model [5–7,13,19], based upon the spin-density matrix

of the PP ensemble,  $\rho$ , which is a  $4 \times 4$  matrix that describes an ensemble of spin- $1/2$  pairs, i.e., a four-level system. The temporal dynamics of  $\rho$ , as well as its magnetic-field dependence, are controlled by the stochastic Liouville equation discussed in detail in Appendix A. Under steady-state conditions, the density matrix is time independent. In terms of the steady-state density matrix,  $\bar{\rho}(B)$ , the singlet and triplet exciton generation rates are given by

$$G_S = r_S \text{tr}[\bar{\rho} P_S], \quad G_T = r_T \text{tr}[\bar{\rho} P_T], \quad (5)$$

where  $r_S$  and  $r_T$  are the singlet and triplet recombination rates of the PP (rather than of the excitons) and  $P_S$  and  $P_T$  are the projection operators onto the singlet and triplet states of the PP.

The influence of a magnetic field in PPR is expected to be small, implying that the field-induced change in generation rates constitutes a small correction to the rates:

$$\delta G_\mu = G_\mu(B) - G_\mu(0) \ll G_\mu(0), \quad \mu = S, T. \quad (6)$$

Here, and in the following, we use  $\delta$  to designate the magnetic-field effect on physical quantities, i.e., changes in physical quantities induced by the magnetic field. Naturally, the magnetic-field effect in singlet and triplet generation is anticorrelated, which has been confirmed experimentally [2] and is described by the relation derived in Appendix A,

$$\left(1 + \frac{r_d}{r_S}\right) \delta G_S + \left(1 + \frac{r_d}{r_T}\right) \delta G_T = 0, \quad (7)$$

with  $r_d$  the dissociation rate of the PP.

The singlet-triplet mixing is the essential constituent of the PPR model. The mixing can result from the difference of precession frequencies of the individual spins in their respective local magnetic environments under the influence of external magnetic field. This difference, in turn, can come from the hyperfine coupling of polaron and nuclear spins, as well as from the different  $g$  factors of electron and hole polarons,  $\Delta g$ . Hence, the hyperfine-field-induced and the  $\Delta g$ -induced singlet-triplet mixing mechanisms can be distinguished [6,23,24]. In our analysis, however, we neglect the  $\Delta g$  mechanism and consider only the hyperfine mechanism. This approach relies on estimates using the reported measured and calculated parameter values of spin mixing by spin-orbit coupling ( $\Delta g$  effect) [15,24,25], showing the dominance of the hyperfine-induced mixing over the  $\Delta g$  mechanism in the magnetic field domain of interest. In addition, this choice stems from the desire to choose the most minimal model, i.e., the model with the least number of parameters, to comprehensively describe the experimental findings.

### B. Triplet-triplet annihilation (TTA) model

A fusion reaction of two triplet excitons has three possible outcomes: the creation of a triplet, the creation of a singlet, and the dissociation back into two triplets, with or without the intermediate formation of a metastable quintet state. In agreement with these possibilities, the rate  $\Gamma$  in Eq. (1) combines the creation of a triplet and dissociation back into two triplets, whereas  $\Phi$  in Eq. (2) gives the rate of singlet creation. These rates are  $B$  dependent because the triplet-triplet reaction is spin conserving and the total spin multiplicity of a pair of

triplets involved in the reaction is field dependent. We quantify this dependence within the TTA model [5,10] in terms of the spin density matrix  $\varrho$  of the triplet-pair ensemble, which is a  $9 \times 9$  matrix for an ensemble of nine-level systems of spin-1 pairs. A detailed description of the model is given in Appendix B.

The triplet-triplet interaction rates  $\Gamma$  and  $\Phi$  are found by considering the triplet balance in the steady state (see Appendix B). The rates are expressed through the steady-state spin-density matrix  $\bar{\varrho}(B)$  as

$$\begin{aligned}\Gamma &= 2k_1k_S\text{tr}[\bar{\varrho}\Pi_S] + k_1k_T\text{tr}[\bar{\varrho}\Pi_T], \\ \Phi &= k_1k_S\text{tr}[\bar{\varrho}\Pi_S],\end{aligned}\quad (8)$$

where  $k_1$  is the triplet-triplet reaction rate,  $k_S$  and  $k_T$  are the singlet and triplet exciton creation rates, and  $\Pi_S$  and  $\Pi_T$  are the projection operators onto the singlet and triplet manifolds of the triplet-pair spin.

Unlike in the case of the PPR model, it is not necessary to restrict our analysis to small magnetic-field effects for TTA because Eq. (4) is linear in either  $\Phi$  or  $(\Phi/\Gamma)$ . In view of Eq. (6) and the fact that the MEL is proportional to the change in singlet-exciton density,  $\delta\bar{S}$ , from Eq. (4) we have

$$\text{MEL} \propto \delta G_S + \delta G_T \left[ \frac{2\xi\Phi}{\Gamma} \right] + \delta\Phi \left[ \frac{G_T\xi}{\Gamma} \right], \quad \xi \ll 1, \quad (9)$$

$$\text{MEL} \propto \delta G_S + \delta G_T \left[ \frac{\Phi}{\Gamma} \right] + \delta \left( \frac{\Phi}{\Gamma} \right) G_T, \quad \xi \gg 1. \quad (10)$$

It should be noted that in the first regime, Eq. (9), the contribution of  $\delta G_T$  is suppressed because  $\Gamma \geq 2\Phi$  as follows from Eq. (8). Hence, the overall contribution of PPR in MEL in this regime is expected to be stronger than in the opposite regime of Eq. (10), where, by virtue of Eq. (7), the first term is offset by the second one. Also note that  $\tau_T$  is treated as field independent, for the reason discussed in the following section.

### C. Triplet-polaron interaction (TPI) model

Yet another process of spin-conserving recombination can occur at an encounter of a triplet exciton and a polaron, from the doublet manifold of the triplet-polaron total spin state. Just as for PPR and TTA, TPI can be sensitive to the external magnetic field because of the field dependence of constituent spin states [5,6,11–14,26], and, if relevant, the field dependence of the TPI would render the triplet lifetime  $\tau_T$  itself field dependent. Therefore, it is reasonable to examine whether the observed triplet features in the MEL can be explained by the TPI mechanism. To address this question, we have created a numerical code for the calculation of the TPI-induced magnetic-field effect, utilizing a density-matrix approach much like those used for the PPR- and TTA-induced field effects. Having covered a wide domain of reasonable parameter space, however, we have concluded that quality fits of the observed MEL can be achieved only by involving substantial contributions of TTA. The TPI mechanism is, therefore, in the context of the present experiments, redundant. This conclusion is detailed in the following section.

## V. COMPARISON OF THEORY AND EXPERIMENT

The best agreement with the experimental MEL results is achieved on the basis of Eq. (9), corresponding to the regime of weaker triplet-triplet interaction,  $\xi \ll 1$ . Hence, to facilitate the following discussion, we combine Eqs. (7) and (9) and write

$$\text{MEL} = A_1 \frac{\delta G_S(B)}{G_S(0)} + A_2 \frac{\delta\Phi(B)}{\Phi(0)}. \quad (11)$$

The two coefficients in Eq. (11) are defined up to an unknown, positive common factor  $A_0$  as

$$A_1 = A_0 \left[ \frac{\Gamma}{2\xi\Phi} - \frac{r_T(r_S + r_d)}{r_S(r_T + r_d)} \right], \quad A_2 = \frac{A_0}{2} \frac{G_T}{G_S}. \quad (12)$$

Here, all quantities are taken at zero field, so  $A_1$  and  $A_2$  are field independent.

In the following, we employ Eq. (11), with  $G_S$  and  $\Phi$  calculated numerically from the PPR and TTA models, to simulate the experimental MEL lines. Besides the rate constants and other intrinsic parameters defining the two models,  $A_1$  and  $A_2$  (or, equivalently,  $A_0$  and  $\xi$ ) are determined from the procedure of finding the best match between simulation and experiment.

### A. Current dependence of h-MEH-PPV MEL

The low-temperature MEL of a h-MEH-PPV OLED at different currents is shown in Fig. 4 together with the simulation results. The MEL response is characterized by a sharp fall in the low-field domain,  $|B| \leq 5$  mT, followed by  $\sim 70$ -mT-wide ‘‘humps’’ centered around  $\pm 50$  mT, which slowly decrease at the higher fields probed, up to  $|B| \leq 230$  mT. Such a field dependence can be interpreted within the theory developed above and summarized in Eq. (11) by linking the initial sharp drop in MEL to the contribution from PPR and the subsequent broader MEL features to the TTA process. This interpretation relies upon the observation that the PPR component—the  $\sim \delta G_S$  term in Eq. (11)—is basically a sharp function of the field, fully saturated at  $|B| \gtrsim 10$  mT, whereas the TTA contribution, the  $\sim \delta\Phi$  term in Eq. (11), is expected to have a wider spread because of the triplets responsible for the effect, which are characterized by zero-field parameters of typically a few tens of microteslas in magnitude [16,27]. Our numerical simulations of the microscopic PPR and TTA models confirm this qualitative picture, yielding excellent agreement between experiment and theory as illustrated in Fig. 4.

From previous studies, the hyperfine-field (hf) strengths of h-MEH-PPV [25,28] as well as the triplet zero-field parameters [16] are known. The four simulated MEL results in Fig. 4 are calculated using these hf strengths for the electron (e) and hole (h),  $B_{\text{hf,e}} = 0.192$  mT and  $B_{\text{hf,h}} = 0.722$  mT, and the triplet-exciton zero-field parameters,  $D = 62$  mT and  $E = 10$  mT, which are very close to the values reported previously [16]. This consistency of the parameters is in direct support of our theoretical interpretation. At the same time, the PPR rate constants are kept the same because the effect of a slight variation of these parameters in  $G_S$  appears to be indistinguishable from balancing changes of  $A_1$ . In general, current-induced effects can be accounted for in spin-dependent recombination models by introducing a current dependence in the rate

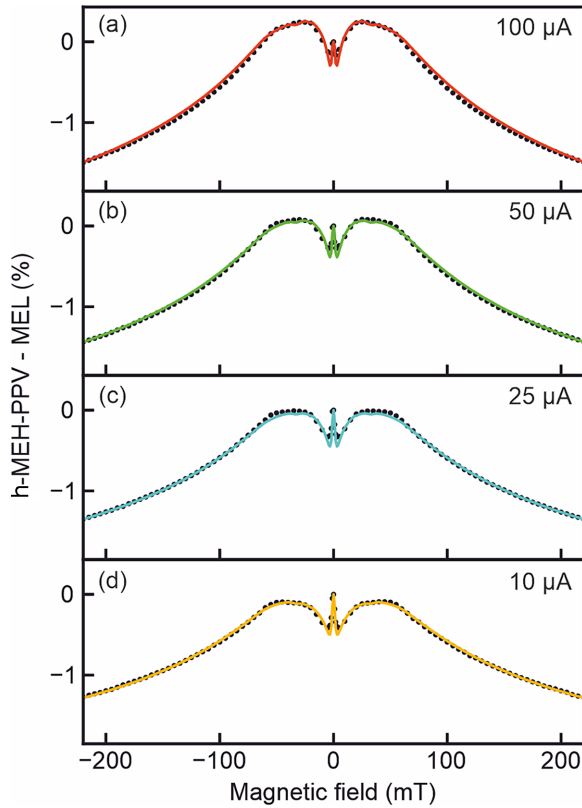


FIG. 4. MEL response of a h-MEH-PPV OLED (dots) recorded at 1.5 K and under (a) 100  $\mu\text{A}$ , (b) 50  $\mu\text{A}$ , (c) 25  $\mu\text{A}$ , and (d) 10  $\mu\text{A}$  constant current. Model simulations (smooth lines) are based on Eq. (11), where  $\delta G_S$  is calculated from the PPR model with hyperfine-field strengths  $B_{\text{hf},e} = 0.192$  mT,  $B_{\text{hf},h} = 0.722$ , and  $\delta\Phi$  is calculated from the TTA model with triplet-exciton zero-field parameters  $D = 62$  mT,  $E = 10$  mT. The remaining parameters are listed in Table I.

constants [6,19,29,30]. For different current values in Fig. 4, slightly different TTA rate constants and coefficients  $A_1$  and  $A_2$  are used, as summarized in Table I.

The triplet-pair spin dynamics is sensitive to the relative orientation of triplet excitons within the pairs. The functional form of the MEL in Fig. 4 is accurately reproduced by theory under the restriction that triplet excitons undergo annihilation if their symmetry axes are only slightly tilted from each other. In other words, we assume that the TTA reaction rate is strongly suppressed if the angle between the symmetry axes of triplets involved exceeds a particular value. This restriction is mathematically formulated by constraining the Euler angles rotating one of the triplets onto the other one in a pair to take values within a narrow domain,  $(-\vartheta, \vartheta)$ , with the maximal tilt angle  $\vartheta$  chosen to optimize the agreement between simulation and experiment. The simulation results in Fig. 4 are calculated with  $\vartheta = 10^\circ$ . We note that relaxing this constraint and taking a full powder average, i.e., averaging over all angles of triplet axes, with the zero-field parameters listed above or close to these values, produces a monotonically decreasing MEL response, very different from what is observed in the experiment. In the following, we return to this important issue and discuss it in detail.

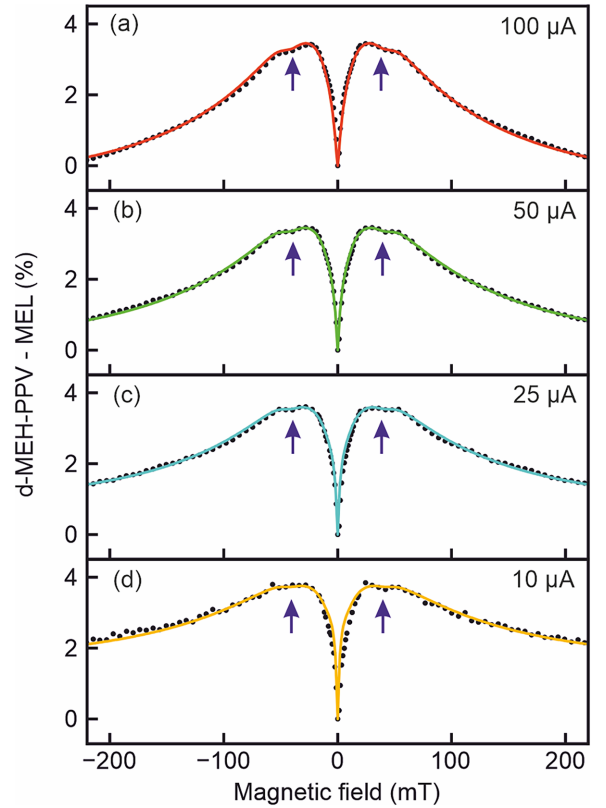


FIG. 5. MEL response of a d-MEH-PPV OLED (dots) recorded at 1.5 K and a constant current of (a) 100  $\mu\text{A}$ , (b) 50  $\mu\text{A}$ , (c) 25  $\mu\text{A}$ , and (d) 10  $\mu\text{A}$ , together with the simulations (smooth lines). Blue arrows point to the dips in MEL consistently seen around  $\pm 43$  mT. This feature is accurately reproduced by the simulations. Parameter values used in the simulations are listed in Table I.

### B. Current dependence of d-MEH-PPV MEL

According to the foregoing analysis, the MEL in the low-field region is dominated by the PPR contribution, which in turn is a function of the polaron hyperfine-field strengths. Further investigation of devices with a d-MEH-PPV emissive layer confirms this conclusion and provides a more insightful picture of the field-dependent processes relevant in these OLEDs.

Figure 5 shows the MEL response of an OLED with an emissive d-MEH-PPV layer, measured at 1.5 K and various currents. Each simulated line in Fig. 5 comprises a narrower PPR component, saturating at approximately 10 mT, and a wider TTA component, which does not appear to saturate over the range of fields considered. The initial sharp drop of the MEL signal is therefore attributed mainly to the PPR components of the model. On the other hand, the shoulders at around  $\pm 50$  mT are signatures of the triplet exciton and arise as TTA features exclusively in the model.

For all the simulations of MEL at different currents in Fig. 5, we employed the hf strength measured for d-MEH-PPV using magnetic-resonance spectroscopy [3,15],  $B_{\text{hf},e} = 0.091$  mT,  $B_{\text{hf},h} = 0.288$  mT. In addition, we assumed triplet-exciton zero-field parameters of  $D = 58$  mT and  $E = 19$  mT, providing the best match between simulation and experiment. The main reason for the apparent differences in shape of the

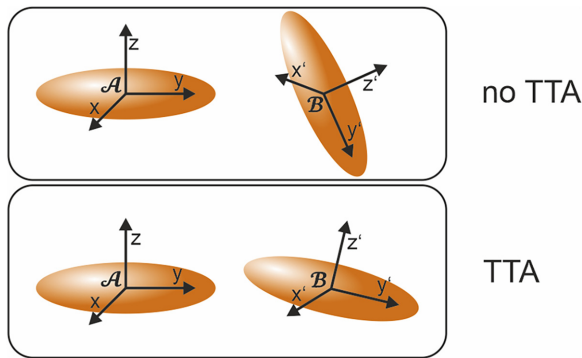


FIG. 6. Schematic of two triplet pairs, formed by triplets  $\mathcal{A}$  and  $\mathcal{B}$  within the black frames, with their respective local symmetry axes. Our findings suggest that TTA is efficient among the pairs with constrained triplet-triplet tilt angles.

MEL response in Figs. 4 and 5 is the sign of the respective PPR components, which is positive for d-MEH-PPV and negative for h-MEH-PPV OLEDs. As discussed in Appendix A, this sign is determined by the relative strength of singlet and triplet recombination rates of the corresponding PPR processes. In particular, we have  $r_S < r_T$  for d-MEH-PPV and  $r_S > r_T$  for h-MEH-PPV. This marked difference may seem surprising, but we note that it is quite conceivable that the deuteration could have an influence on polymer chain morphology in the bulk film, which may affect recombination rates. Also, it has previously been proposed that deuteration can affect charge transport due to an influence of nuclear tunneling in the microscopic hopping process [31]. If this is indeed the case, then the final hopping step in carrier recombination could also be impacted by deuteration. In any case, we stress that this reversal of the spin-dependent rates is not a consequence of the modeling but is apparent from the raw experimental data, with the inversion of the narrow peak around zero field occurring upon deuteration. A thorough understanding of the effect will require quantum chemical modeling following the approach of Jiang *et al.* [31].

As before, acceptable agreement of the calculated and measured MEL lines, including the specific dips in MEL marked in Fig. 5 by blue arrows, is achieved with the TTA model under the constraint that triplet pairs undergo annihilation only if the angle between their symmetry axes is small. A schematic of this constraint is given in Fig. 6. Besides the overall high level of agreement between simulation and measurement, this conclusion is supported by the following argument. Our analysis in Appendix C shows that the shallow dips in the MEL at around  $\pm 43$  mT in Fig. 5 result from triplet-pair level-crossing resonances [10,11]. The location of such a level crossing depends on the angle between the symmetry axes of the two triplets. Hence, the resulting feature is smeared out and not discernible if a full powder average, i.e., an average over all possible angles of mutual orientation of the two triplets, is involved. Therefore, the clear presence of the dip feature in the MEL provides an indication of partial but not complete averaging over the angle between symmetry axes of the individual triplet excitons.

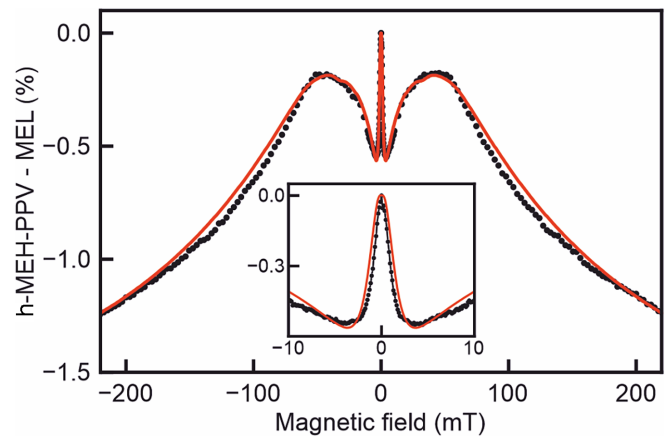


FIG. 7. MEL of a h-MEH-PPV OLED recorded at 1.5 K and 100  $\mu$ A constant current, measured with a higher field resolution of 110  $\mu$ T from  $-11$  to 11 mT. Due to the higher resolution, the central peak (magnified in the inset) appears sharper and more pronounced as compared to the lower-resolution data in Fig. 4. Nevertheless, the model simulations reproduce the measurement.

It is also worth noting that the triplet-pair level-crossing resonance features appear to be weaker in the MEL lines calculated for the h-MEH-PPV and, consistent with this observation, are not as well resolved in the experiment.

### C. High-resolution MEL of a h-MEH-PPV OLED

The nonmonotonic nature of the narrow MEL field dependence in Fig. 4 raises the question of how accurately the reference point for the MEL, the EL intensity at zero field, can be determined. The use of superconducting magnets in this study followed from previous work done at high magnetic fields of up to 8 T, which motivated the current study [8]. Superconducting magnets are designed to generate large fields but are not optimized for sweeps over small field ranges. In particular, the supercurrents have to be actively dissipated or else hysteretic effects will arise. The precision with which the zero-field EL intensity can be determined will control the amplitude of the maximum in the nonmonotonic MEL of h-MEH-PPV. The field sweeps in Fig. 4 were performed with an accuracy of 1 mT, averaged over 20 repeats of the measurement. While the zero-field peak in the MEL is clearly resolved, its amplitude relative to the broader MEL features is likely to be reduced due to the limited resolution, which arises from obvious constraints on measurement time. To assess this issue, we performed high-resolution MEL measurements, with an almost tenfold increase in magnetic-field resolution as shown in Fig. 7. Under these measurement conditions, the narrow peak of the MEL at zero field is indeed increased compared to the results of Fig. 4. Nevertheless, accurate agreement with the simulation using the same parameters as in Fig. 4 is found, albeit with a slight increase in the relative amplitude of the PPR contribution over the TTA contribution. This agreement demonstrates that, to a first approximation, matching the experimental and simulated MEL is independent of measurement resolution, provided that the resolution is sufficient so that the narrow peak due to PPR can be resolved.

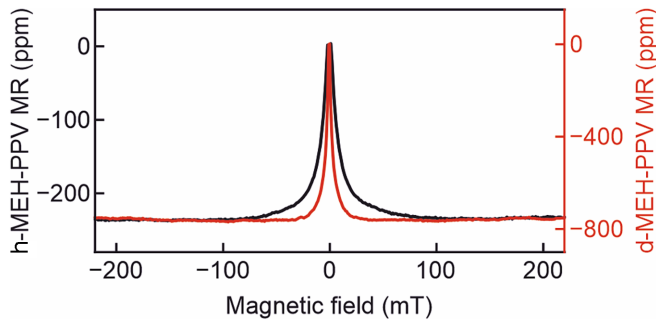


FIG. 8. Magnetoresistance of h-MEH-PPV and d-MEH-PPV OLEDs recorded at 1.5 K and 50  $\mu$ A constant current.

#### D. Magnetoresistance: Elimination of the TPI mechanism

Another basic mechanism that can lead to magnetic-field effects in experimental observables, including the current and the luminescence, is TPI [6,11–14,26]. Without violating spin-selection rules, recombination of a triplet exciton and a polaron can occur from the doublet state of a pair of a triplet exciton and a polaron. This state underlies the TPI mechanism, as the externally applied field can change the spin states of the exciton and the polaron, perturbing the total spin of the pair.

The two possible pathways of recombination due to TPI are (i) the quenching of a triplet exciton with the transfer of its energy to the polaron [6,11,12,26] and (ii) the spin-conserving up-conversion of a triplet exciton into a higher-energy singlet exciton, at the expense of polaron kinetic energy [13,14]. Thus, scenario (i) can result in a reduction and scenario (ii) in an increase of the device resistance. On the other hand, scenario (i) can directly affect the emission intensity from a phosphorescent OLED whereas scenario (ii) impacts the fluorescence [13,14].

Our efforts to apply the TPI mechanism instead of the TTA mechanism in simulating the MEL, involving extensive simulations not shown here, resulted in insufficient agreement between theory and measurement, leading us to conclude that, in the parameter domain under consideration, the TPI mechanism of magnetic-field effects is not substantial in the case of the OLEDs studied here. That said, we do not exclude the presence of TPI as a source of triplet quenching, particularly the energetically more plausible scenario (i), which will contribute to the triplet lifetime  $\tau_T$ . However, we are not able to discern any credible signatures in the MEL of a field dependence of the TPI.

The foregoing conclusion is further supported by the fact that the magnetoresistance measured for both d-MEH-PPV and h-MEH-PPV devices at different currents, illustrated in Fig. 8, unlike to the MEL in Figs. 4 and 5, shows no discernible feature on the field scale of the triplet-exciton zero-field parameters, i.e.,  $\pm 43$  mT. The TPI mechanism is expected to have a direct impact on the device magnetoresistance, whereas the TTA mechanism is not since it does not directly involve charge carriers. Although we note that any field-induced change in triplet population, including that originating from TTA, may show up in transport because triplets can act as charge-scattering centers, it evidently does not

the present case. We therefore exclude the TPI mechanism as an explanation of the MEL for the materials and devices in the current study.

## VI. DISCUSSION

Besides free charge carriers and fluorescent singlet excitons, triplet excitons are essential to the operation of organic optoelectronic devices. It is therefore important to understand, and potentially control, mechanisms involving triplets, particularly the spin-conserving TPI and TTA processes that can have a substantial impact on the lifetime of triplets. These two processes often have similar fingerprints and are difficult to distinguish from simple measurements of MEL. A natural way to determine the relative importance of these two mechanisms of triplet quenching is to exploit their linear (TPI) versus quadratic (TTA) dependence on triplet density [32]. The triplet density is related to the strength of primary excitation, which in turn is controlled by the injected current density in the case of EL. However, other factors such as recombination cross sections and the charge imbalance can also play a decisive role in changing the relative importance of TPI and TTA in either direction. In Ref. [21], for example, TPI was found to be the dominant field-dependent triplet decay channel at low temperatures in an electron-rich MEH-PPV-based OLED.

In our experiment, OLEDs are operated under relatively high constant currents to allow for an optimal signal-to-noise ratio. At these high currents, at low temperatures, a regime is realized where TTA is indeed the dominant magnetic-field-dependent channel of triplet quenching, as follows from our theoretical analysis. In this regime, the PPR- and TTA-induced magnetic-field effects are of comparable magnitude, but since the rate of TTA depends on the square of the triplet density, the maximal effect amplitude relating to TTA increases with increasing current as seen in Fig. 3. It is instructive to compare the change of the dynamic range of the MEL from  $B = 50$  mT to  $B = 220$  mT, the span of the MEL amplitude controlled by TTA: for the protonated compound, this range increases continuously from 1.2% to 1.7% as the current is raised by an order of magnitude; for the deuterated compound, the range increases from 1.7% to 3.2%. Perhaps surprisingly, the model calculations accurately reproduce the experimental data *only* if TTA is restricted to a subensemble of triplet pairs with small tilt angles between their symmetry axes. Presumably, this apparent ordering of triplet axes is related to the dependence of the degree of overlap between the two triplet wavefunctions on the angle between the two triplet axes, resulting from the nontrivial spatial extent of the wavefunctions. Our comprehensive theoretical investigation of TTA with such angular confinement (not shown here) reveals a strong resemblance of magnetic-field effects resulting from TTA with those arising from TPI under the condition that the triplets are orientated preferentially along the direction of the magnetic field. Obviously, there is no rationale why there should be such a high degree of ordering of triplet states in an amorphous material such as a spin-coated polymer film. Thus, TTA with angular constraints *between* triplets but *not of* the triplets offers a suitable explanation for the magnetic-field

effects reported previously in organic semiconductor materials that have been interpreted by including a preferential microscopic orientation of triplets along the magnetic-field lines [33,34].

In the previous study [8], TSP was found to be responsible for the low-temperature MEL effect at magnetic fields several teslas in strength, in OLED structures very similar to those studied here but with different emissive materials. We note that the TSP effect is irrelevant in the field domain under consideration. In particular, a simple estimate based on the approach of Ref. [7] shows the TSP effect is of order  $10^{-6}$  at  $|B| \lesssim 200$  mT, i.e., three orders of magnitude weaker than that of the PPR and TTA effects considered here. Besides, both the PPR and the TTA mechanisms are based upon the spin-dependent recombination, which is irrelevant to TSP [5]. We concede that, in our work on TSP, we argued in passing that the temporal decay and the bias dependence of transient EL at low temperatures in rather similar devices did not provide a direct indication of delayed fluorescence arising from TTA, which previously led us to the conclusion that TPI should be of the greater significance in MEL than TTA [8]. This qualitative reasoning was evidently not entirely correct, although TPI has indeed previously been established unambiguously in similar device structures at low temperatures by pulsed electrically detected magnetic resonance (pEDMR) spectroscopy [21]. We conclude that both TTA and TPI can therefore potentially play a role in the MEL response, although in the present study, the MEL must clearly be dominated by TTA. We also note that, in the face of charge trapping in the OLED at low temperatures [35], time-resolved EL may not be the most effective probe of delayed fluorescence generated by TTA. Instead, in future experiments, a modulation of the MEL amplitude, e.g., by modulating the OLED current, is called for in order to identify the relevant timescales, which are presumably limited by the triplet lifetime. In addition, building on the work of Partee *et al.* [32], the modulated MEL response should be carefully analyzed in terms of in-phase, out-of-phase (i.e., quadrature), and second harmonic signatures. This analysis will allow a direct distinction between TPI and TTA, which depend linearly and quadratically, respectively, on triplet density. Finally, it should also be possible to probe the MEL under radiofrequency excitation *resonant* with the triplet state (i.e., optically detected magnetic resonance), although it will be challenging at the low magnetic fields and low temperatures involved to couple the OLED to a suitable source of radio-frequency radiation.

#### ACKNOWLEDGMENTS

This work was supported by the Deutsche Forschungsgemeinschaft (DFG, German Research Foundation), Project ID 314695032–SFB 1277, Subproject No. B03. The synthesis of the perdeuterated monomer took place at the Australian National Deuteration Facility, which is partly funded by NCRIS, an Australian Government initiative. P.L.B. acknowledges support as an Australian Research Council Laureate Fellow, and the synthesis work was supported in part by this Fellowship (FL160100067).

#### APPENDIX A: MICROSCOPIC DESCRIPTION OF THE PPR MODEL

The time evolution of the PPR density matrix  $\rho$  is described by the stochastic Liouville equation,

$$\frac{d\rho}{dt} = \mathcal{R}_{\text{dr}}(\rho) + \mathcal{R}_{\text{sr}}(\rho) + \frac{1}{4}\Lambda_{\text{PP}}\mathbb{1}_{4\times 4} + i[\rho, H_{\text{PP}}], \quad (\text{A1})$$

where  $\mathcal{R}_{\text{dr}}$  denotes the dissociation and recombination,  $\mathcal{R}_{\text{sr}}$  denotes the spin relaxation, the third term is the PP source term, with the generation rate  $\Lambda_{\text{PP}}$  (the factor  $1/4$  accounts for the spin multiplicity and  $\mathbb{1}_{4\times 4}$  is the  $4 \times 4$  identity matrix), and the last term governs the coherent spin dynamics due to the PP spin Hamiltonian,  $H_{\text{PP}}$ . Note that Eq. (A1) is a  $4 \times 4$  matrix differential equation.

The dissociation and the recombination are defined in terms of the phenomenological rate constants introduced in the main text. We assume a uniform, spin-independent dissociation of pair states back into free polarons, and spin-conserving recombination. This assumption is written as

$$\mathcal{R}_{\text{dr}}(\rho) = -r_{\text{d}}\rho - (r_{\text{S}}/2)\{\rho, P_{\text{S}}\} - (r_{\text{T}}/2)\{\rho, P_{\text{T}}\}, \quad (\text{A2})$$

where  $\{, \}$  denotes the anticommutator.

We work in the regime of slow effective spin relaxation, so the spin dynamics are predominantly governed by the coherent and the recombination-dissociation processes. Moreover, the effect of spin relaxation is often indistinguishable from that of recombination-dissociation processes, and therefore we neglect most of the spin relaxation channels. However, as noted earlier, the MEL linewidth around zero field due to the PPR process is quite sensitive to the singlet-triplet dephasing caused by the modulation of the exchange interaction between the two polaron states in a pair [36]. Hence, we retain only this spin relaxation (sr) with the term

$$\mathcal{R}_{\text{sr}}(\rho) = -\frac{1}{T_{\text{sr}}}(P_{\text{S}}\rho P_{\text{T}} + P_{\text{T}}\rho P_{\text{S}}). \quad (\text{A3})$$

The spin-relaxation time,  $T_{\text{sr}}$ , is expected to be of the order of 500 ns [27,37].

The source term in Eq. (A1) is proportional to the free electron and hole densities,  $\Lambda_{\text{PP}} \propto n_{\text{e}}n_{\text{h}}$ . It is assumed that the field dependence of PPR induces only a negligible change in the polaron densities, so  $\Lambda_{\text{PP}}$  is taken as a field-independent constant.

Singlet and triplet exciton generation rates, Eq. (5) in the main text, are defined through the steady-state density matrix,  $\bar{\rho}$ . By taking the trace of Eq. (A1) in the steady state, one arrives at

$$(r_{\text{d}} + r_{\text{T}})\text{tr}(\bar{\rho}P_{\text{T}}) + (r_{\text{d}} + r_{\text{S}})\text{tr}(\bar{\rho}P_{\text{S}}) = \Lambda_{\text{PP}}, \quad (\text{A4})$$

where the relation  $P_{\text{T}} + P_{\text{S}} = \mathbb{1}_{4\times 4}$  is used. Equation (7) of the main text follows from Eqs. (5) and (A4). To discuss the sign of the MEL due to PPR, we use Eqs. (5) and (A4) to write

$$\delta G_{\text{S}} = \frac{r_{\text{S}}(r_{\text{d}} + r_{\text{T}})}{r_{\text{T}} - r_{\text{S}}}\delta[\text{tr}(\bar{\rho})]. \quad (\text{A5})$$

Now,  $\text{tr}(\bar{\rho})$  is the steady-state population of PPs, and the field-induced change in this quantity is expected to be positive,

$$\delta[\text{tr}(\bar{\rho})] \geq 0. \quad (\text{A6})$$

TABLE I. Parameters used in the MEL model simulations shown in Figs. 4, 5, and 7.

	Parameter	h-MEH-PPV					d-MEH-PPV				
		Fig. 4(a)	Fig. 4(b)	Fig. 4(c)	Fig. 4(d)	Fig. 7	Fig. 5(a)	Fig. 5(b)	Fig. 5(c)	Fig. 5(d)	
TTA	$k_d$ (MHz)	1.0	1.2	1.9	3.0	6.0	30	30	55	81	
	$k_S$ (MHz)	600	700	840	1200	2000	2400	3000	4200	6600	
	$k_T$ (MHz)	200	200	200	200	230	1300	1300	1300	6000	
	$D$ (mT)	62					58				
	$E$ (mT)	10					19				
	$D_{\text{dip}}$ (mT)	1.0					0.0				
	$J$ (mT)	1.0					1.0				
	PPR	$r_d$ (kHz)	800					80			
		$r_S$ (kHz)	800					80			
		$r_T$ (kHz)	700					84			
$B_{\text{hf,e}}$ (mT)		0.192					0.091				
$B_{\text{hf,h}}$ (mT)		0.722					0.288				
$T_{\text{sr}}$ (ns)		500					500				
$D_{\text{dip}}$ (mT)		0.22					0.22				
$J$ (mT)		0.04					0.04				

This assumption arises because the external field basically slows down the hyperfine-induced singlet-triplet mixing, by effectively screening the hyperfine interaction, and once the two (singlet and triplet) reservoirs are more isolated, the total population goes up. From Eqs. (A5) and (A6), the sign of  $\delta G_S$  is readily seen to be positive for  $r_T > r_S$ , and negative in the opposite case, in agreement with the result of Ref. [19].

We note in passing that Eq. (A6) implies a field-induced growth in the PP dissociation rate,  $r_d \text{tr}(\bar{\rho})$ , leading to an increasing free charge-carrier density and thus to negative magnetoresistance, independent of the recombination rates.

The PP Hamiltonian  $H_{\text{PP}}$  includes the hyperfine, Zeeman, dipolar, and exchange interactions,

$$H_{\text{PP}} = H_{\text{PP,hf}} + H_{\text{PP,Zeeman}} + H_{\text{PP,dip}} + H_{\text{PP,ex}}. \quad (\text{A7})$$

We utilize the semiclassical approach to the hyperfine interaction, described by local static random magnetic fields of a Gaussian distribution with zero mean, independent from site to site. Random hyperfine fields acting on the electron and hole polaron spins are of different characteristic strengths,  $B_{\text{hf,e}}$  and  $B_{\text{hf,h}}$ . The Cartesian coordinates of the local hyperfine fields  $b_{i,\mu}$ , with  $i = x, y, z$ , and  $\mu = e, h$ , are thus random variables following a Gaussian distribution,  $N(b_{i,\mu}) = (2\pi B_{\text{hf},\mu}^2)^{-1/2} \exp(-b_{i,\mu}^2/B_{\text{hf},\mu}^2)$ . The PP hyperfine interaction is given by the Hamiltonian

$$H_{\text{PP,hf}} = \hbar\gamma(\mathbf{b}_e \mathbf{S}_e + \mathbf{b}_h \mathbf{S}_h), \quad (\text{A8})$$

where  $\gamma$  is the electron (and hole) gyromagnetic ratio, and  $\mathbf{S}_e$  and  $\mathbf{S}_h$  are the electron and hole polaron spin operators. The Zeeman term has the form

$$H_{\text{PP,Zeeman}} = \hbar\gamma \mathbf{B}(\mathbf{S}_e + \mathbf{S}_h), \quad (\text{A9})$$

where  $\mathbf{B}$  is the externally applied magnetic field. The dipolar interaction is described by

$$H_{\text{PP,dip}} = D_{\text{dip}}[\mathbf{S}_e \mathbf{S}_h - 3(\mathbf{S}_e \mathbf{r})(\mathbf{S}_h \mathbf{r})/r^2], \quad (\text{A10})$$

where  $r$  is the displacement vector connecting the two polarons and  $D_{\text{dip}} = (\mu_0 \hbar^2 \gamma^2)/(4\pi r^3)$  is the dipolar coupling

strength with  $\mu_0$  the magnetic permeability. Note that this coupling constitutes a point-dipole approximation, ignoring the spatial extent of the polaron wavefunctions. In the numerical simulations, we assume a fixed polaron-polaron separation, i.e., a fixed dipolar coupling strength, and include disorder only in the orientation of the polaron-polaron displacements. For the exchange coupling, we adopt the isotropic Hamiltonian

$$H_{\text{PP,ex}} = J(\mathbf{S}_e \mathbf{S}_h). \quad (\text{A11})$$

In the organic semiconductors under consideration, one typically has hyperfine fields of less than 1 mT standard deviation, and even weaker average dipolar and exchange coupling strengths,  $|J|/\hbar\gamma, |D_{\text{dip}}|/\hbar\gamma \lesssim 0.3$  mT [38].

The numerical evaluation of the PPR-induced component of the MEL signal is found from the solution of Eq. (A1) under steady-state conditions, which is a  $4 \times 4$  system of algebraic equations. Sets of local hyperfine fields and polaron-polaron displacement orientations are Monte Carlo sampled, according to the respective Gaussian and spherical (spatially isotropic) distributions of these parameters, and the steady-state system of algebraic equations is solved for each set. The density-matrix elements are subsequently found by averaging the individual solutions, and  $G_S(B)$  is calculated by repeating the procedure for discrete  $B$  values. The PPR parameters used in our model simulations are listed in Table I below.

## APPENDIX B: MICROSCOPIC DESCRIPTION OF THE TTA MODEL

The TTA model is described by the density matrix  $\varrho$ , obeying the stochastic Liouville equation,

$$\frac{d\varrho}{dt} = \mathcal{R}_{\text{dr}}(\varrho) + \mathcal{R}_{\text{sr}}(\varrho) + \frac{1}{9} \Lambda_{\text{TT}} \mathbb{1}_{9 \times 9} + i[\varrho, H_{\text{TT}}]. \quad (\text{B1})$$

Here, the dissociation and recombination, and spin relaxation, are described by the terms  $\mathcal{R}_{\text{dr}}$  and  $\mathcal{R}_{\text{sr}}$ , the triplet pair source term comes with the generation rate  $\Lambda_{\text{TT}}$ , and the

coherent dynamics are governed by the triplet-exciton-pair spin Hamiltonian  $H_{\text{TT}}$ . Equation (B1) is thus a  $9 \times 9$  matrix differential equation.

The dissociation-recombination term in Eq. (B1) is defined as

$$\mathcal{R}_{\text{dr}}(\varrho) = -k_{\text{d}}\varrho - (k_{\text{S}}/2)\{\varrho, \Pi_{\text{S}}\} - (k_{\text{T}}/2)\{\varrho, \Pi_{\text{T}}\}. \quad (\text{B2})$$

For the spin relaxation, we utilize a term of the form

$$\begin{aligned} \mathcal{R}_{\text{sr}}(\varrho)_{\alpha\alpha} &= -\frac{1}{T_1} \left[ \varrho_{\alpha\alpha} - \frac{1}{9} \text{tr}(\varrho) \right], \\ \mathcal{R}_{\text{sr}}(\varrho)_{\alpha\beta} &= -\frac{1}{T_2} \varrho_{\alpha\beta}, \quad \alpha \neq \beta. \end{aligned} \quad (\text{B3})$$

The spin relaxation [Eq. (B3)] incorporates the population decay (i.e.,  $T_1$  processes) and the coherence loss ( $T_2$  processes) due to the coupling of triplet spins to environmental degrees of freedom (e.g., vibrations). Referring to Appendix A of Ref. [39], we note that the above form of spin relaxation would follow from the Lindblad formulation of the stochastic Liouville equation, where the so-called system (or jump) operators are defined as  $c_{\alpha\beta} = \gamma_{\alpha\beta}|\alpha\rangle\langle\beta|$ , with  $\gamma_{\alpha\beta} = (1/9T_1)^{1/2}$ ,  $\beta \neq \alpha$ , and  $\gamma_{\alpha\alpha} = (1/T_2 - 8/9T_1)^{1/2}$ .

Our numerical results using Eq. (B3) lead us to conclude that, while the overall signal magnitudes are affected by the spin relaxation, the line shapes are basically preserved, provided the relaxation times are long enough to retain the magnetic-field effect, i.e., on the order of a few hundreds of nanoseconds as seen in our simulations. However, the signal magnitude is balanced by the fit constant  $A_2$  in Eq. (11). Therefore, the spin relaxation does not play an essential role in the line-shape analysis, and the relaxation times cannot be extracted unambiguously from the MEL simulations.

The triplet-pair generation rate is quadratic in the triplet density,  $\Lambda_{\text{TT}} = k_1 T^2$ , where  $k_1$  is the triplet-triplet reaction rate. In the steady state, the process described by Eq. (B1) destroys two triplets with the rate  $\Lambda_{\text{TT}}$ , creates two triplets with the rate  $k_{\text{d}}\text{tr}(\bar{\varrho})$ , creates one triplet with the rate  $k_{\text{T}}\text{tr}(\bar{\varrho}\Pi_{\text{T}})$ , and creates one singlet with the rate  $k_{\text{S}}\text{tr}(\bar{\varrho}\Pi_{\text{S}})$ . Putting these together, we find

$$\begin{aligned} \Gamma T^2 &= 2\Lambda_{\text{TT}} - 2k_{\text{d}}\text{tr}(\bar{\varrho}) - k_{\text{T}}\text{tr}(\bar{\varrho}\Pi_{\text{T}}), \\ \Phi T^2 &= k_{\text{S}}\text{tr}(\bar{\varrho}\Pi_{\text{S}}). \end{aligned} \quad (\text{B4})$$

Another useful relation is found by taking the trace of Eq. (B1):

$$k_{\text{d}}\text{tr}(\bar{\varrho}) + k_{\text{T}}\text{tr}(\bar{\varrho}\Pi_{\text{T}}) + k_{\text{S}}\text{tr}(\bar{\varrho}\Pi_{\text{S}}) = \Lambda_{\text{TT}}. \quad (\text{B5})$$

To simplify the notations, we divide the steady-state Eq. (B1) by  $T^2$  and renormalize the density matrix by absorbing the factor  $\bar{\varrho} \rightarrow \bar{\varrho}/T^2$ . The renormalized  $\bar{\varrho}$  is the density matrix used in the main text. It is the steady-state solution of Eq. (B1) with the generation rate set to  $k_1$ . Equation (8) in the main text is found from Eq. (B4), by replacing  $\Lambda_{\text{TT}}$  with the left-hand side of Eq. (B5).

The spin Hamiltonian of two interacting triplets ( $\mathcal{A}$  and  $\mathcal{B}$ ) in a static magnetic field,  $H_{\text{TT}}$ , upon which the TTA model is based, is composed of four basic interactions:

$$H_{\text{TT}} = H_{\text{TT,Zeeman}} + H_{\text{zfs},\mathcal{A}} + H_{\text{zfs},\mathcal{B}} + H_{\mathcal{A}\mathcal{B}}, \quad (\text{B6})$$

where  $H_{\text{TT,Zeeman}}$  is the Zeeman term induced by the magnetic field,  $H_{\text{zfs},\mathcal{A}}$  and  $H_{\text{zfs},\mathcal{B}}$  are the zero-field splitting Hamiltonians for the triplets  $\mathcal{A}$  and  $\mathcal{B}$ , and  $H_{\mathcal{A}\mathcal{B}}$  is the triplet-triplet spin-coupling term including the magnetic exchange and dipolar interactions.

The Zeeman term has the form

$$H_{\text{TT,Zeeman}} = \hbar\gamma\mathbf{B}(\mathbf{S}_{\mathcal{A}} + \mathbf{S}_{\mathcal{B}}), \quad (\text{B7})$$

where  $\mathbf{S}_{\mathcal{A}}$  and  $\mathbf{S}_{\mathcal{B}}$  are the spin operators of  $\mathcal{A}$  and  $\mathcal{B}$  triplets.

In the following, we use the coordinate frame formed by the zero-field principal axes ( $\mathbf{x}$ ,  $\mathbf{y}$ ,  $\mathbf{z}$ ) of triplet  $\mathcal{A}$ , in which we have

$$\begin{aligned} H_{\text{zfs},\mathcal{A}} &= D[(S_{\mathcal{A}}^z)^2 - 2/3] + E[(S_{\mathcal{A}}^x)^2 - (S_{\mathcal{A}}^y)^2] \\ &= \begin{pmatrix} D/3 & 0 & E \\ 0 & -2D/3 & 0 \\ E & 0 & D/3 \end{pmatrix}, \end{aligned} \quad (\text{B8})$$

with  $D$  and  $E$  the triplet (axial and rhombic) zero-field splitting parameters. The triplet  $\mathcal{B}$  has its principal axes  $\mathbf{x}'$ ,  $\mathbf{y}'$ ,  $\mathbf{z}'$  tilted with respect to the principal axes of triplet  $\mathcal{A}$ . A natural way to describe the relative tilt of the two triplets is via the set of Euler angles  $(\phi, \theta, \psi)$ . Using the  $zx'z''$  convention of the Euler angles [40], and denoting via  $K'$  the matrix with columns  $\mathbf{x}'$ ,  $\mathbf{y}'$ ,  $\mathbf{z}'$ , we have

$$K' = OK, \quad (\text{B9})$$

where  $K$  is the (unit) matrix of columns  $\mathbf{x}$ ,  $\mathbf{y}$ ,  $\mathbf{z}$ , and the rotation matrix has the explicit form

$$O = \begin{pmatrix} c_1c_3 - s_1c_2s_3 & -c_1s_3 - s_1c_2c_3 & s_1s_2 \\ s_1c_3 + c_1c_2s_3 & c_1c_2c_3 - s_1s_3 & -c_1s_2 \\ s_2s_3 & s_2c_3 & c_2 \end{pmatrix}, \quad (\text{B10})$$

with  $c$  and  $s$  denoting cosine and sine functions of arguments  $\phi$ ,  $\theta$ ,  $\psi$ , corresponding to subscripts 1, 2, 3, respectively. The Hamiltonian of the second triplet is found by rotating Eq. (B8) in the spinor space,

$$H_{\text{zfs},\mathcal{B}} = \mathcal{D}^\dagger H_{\text{zfs},\mathcal{A}} \mathcal{D}, \quad (\text{B11})$$

where  $\mathcal{D}(\phi, \theta, \psi)$  is the  $S = 1$  Wigner rotation matrix [the matrix of  $S = 1$  spinor representation of the rotation Eq. (B10)], defined as  $\mathcal{D} = \exp(i\psi S_{\mathcal{A}}^z) \exp(i\theta S_{\mathcal{A}}^x) \exp(i\phi S_{\mathcal{A}}^z)$ . Explicitly, we have

$$H_{\text{zfs},\mathcal{B}} = \begin{pmatrix} U & V & W \\ V^* & -2U & -V \\ W^* & -V^* & U \end{pmatrix}, \quad (\text{B12})$$

where

$$\begin{aligned} U &= D \frac{3\cos^2\theta - 1}{6} - E \frac{\sin^2\theta \cos 2\psi}{2}, \\ V &= i \sin\theta \frac{e^{i\phi}}{\sqrt{2}} [D \cos\theta + E(\cos 2\psi \cos\theta - i \sin 2\psi)], \\ W &= -\frac{e^{-2i\phi}}{2} [D \sin^2\theta - E(\cos 2\psi (1 + \cos^2\theta) \\ &\quad - 2i \sin 2\psi \cos\theta)]. \end{aligned} \quad (\text{B13})$$

The triplet-triplet coupling term  $H_{\mathcal{A}\mathcal{B}}$  includes dipolar and exchange interactions,  $H_{\mathcal{A}\mathcal{B}} = H_{\mathcal{A}\mathcal{B},\text{dip}} + H_{\mathcal{A}\mathcal{B},\text{ex}}$ . For these

interactions, we utilize forms of Eqs. (A10) and (A11), with  $\mathbf{S}_e, \mathbf{S}_h$  replaced by  $\mathbf{S}_A, \mathbf{S}_B$ .

Just as in the case of PPR, the numerical evaluation of the TTA-induced components of the MEL response is based on Monte Carlo sampling of a set of parameters including the two triplet zero-field symmetry axes, the direction of the magnetic field, and the orientation of the vector describing the displacement of the two triplets. The steady-state system of the  $9 \times 9$  algebraic equations is then solved for each set of parameters, and the density matrix is found as the average of the solutions over the samplings, for different values of  $B$ . The observables  $\Phi(B)$  and  $\Phi(B)/\Gamma(B)$  are calculated from Eq. (8). The TTA parameters used in simulations are listed in Table I.

### APPENDIX C: TRIPLET LEVEL-CROSSING RESONANCES

At certain field orientations and field strengths, some triplet-pair energy levels can cross each other. Because of the degeneracy, the population mixing of the states involved can be enhanced resonantly, leading to an increase or decrease in the rate of triplet fusion. These kinds of level-crossing resonances are known to occur in systems with ordered triplet excitons and have been observed in the delayed fluorescence of some organic crystals [10,11]. In amorphous systems such as conjugated polymers with an isotropic distribution of triplet orientations, however, the level-crossing resonance features would be expected to be completely smeared out due to the angular dependence of level-crossing positions in space with respect to the magnetic-field orientation.

The fine structure in low-temperature MEL reported in this work is clearly reproduced under the assumption of restricted tilt angles between the two triplets undergoing fusion. We attribute the observed fine structure to level-crossing resonances, which are not completely smeared out because of the restricted triplet-triplet tilt angle. In order to further elucidate this issue, we examine our framework of TTA for the existence of level crossings and their potential dependence on magnetic-field orientation and relative triplet-triplet tilt angle.

The eigenvalues of the Hamiltonian of triplet  $\mathcal{A}$  in the magnetic field

$$H_{\mathcal{A}} = \hbar\gamma\mathbf{B}\mathbf{S}_{\mathcal{A}} + H_{zfs,\mathcal{A}} \quad (\text{C1})$$

are given by the secular equation

$$\epsilon^3 - \epsilon[\beta^2 - (XY + XZ + YZ)] + \beta_x^2 X + \beta_y^2 Y + \beta_z^2 Z - XYZ = 0, \quad (\text{C2})$$

where  $\boldsymbol{\beta} = \hbar\gamma\mathbf{B}$  is the magnetic field on an energy scale and  $\beta_i$ ,  $i = x, y, z$ , are the projections of  $\boldsymbol{\beta}$  onto the triplet principal axes ( $\beta_i = \beta \cos\alpha_i$ , where  $\alpha_i$  is the angle made by  $B$  with the  $i$ th principal axis), and

$$X = \frac{1}{3}D - E, \quad Y = \frac{1}{3}D + E, \quad Z = -\frac{2}{3}D \quad (\text{C3})$$

are the eigenvalues of the zero-field Hamiltonian  $H_{zfs,\mathcal{A}}$ , corresponding to the eigenstates

$$|x\rangle = \frac{1}{\sqrt{2}}(T_+ - T_-), \quad |y\rangle = \frac{i}{\sqrt{2}}(T_+ + T_-), \quad |z\rangle = T_0. \quad (\text{C4})$$

For the Hamiltonian  $H_{\mathcal{B}} = \hbar\gamma\mathbf{B}\mathbf{S}_{\mathcal{B}} + H_{zfs,\mathcal{B}}$  of triplet  $\mathcal{B}$ , one arrives at a secular equation given by Eq. (C2), where  $\boldsymbol{\beta}$  is replaced by  $\boldsymbol{\beta}' = \mathcal{O}^\dagger\boldsymbol{\beta}$ .

The roots of Eq. (C2) can be found analytically and expressions can be written for the energy levels of  $H_{\mathcal{A}}$ , for arbitrary field orientations, as

$$\begin{aligned} \epsilon_{\mathcal{A},1} &= 2\sqrt{Q}\cos(\lambda/3), \\ \epsilon_{\mathcal{A},2} &= 2\sqrt{Q}\cos([\lambda + 2\pi]/3), \\ \epsilon_{\mathcal{A},3} &= 2\sqrt{Q}\cos([\lambda + 4\pi]/3), \end{aligned} \quad (\text{C5})$$

where  $Q = [\beta^2 - (XY + XZ + YZ)]/3$  and  $\lambda = \arccos(R/\sqrt{Q^3})$ , with  $R = (XYZ - \beta_x^2 X - \beta_y^2 Y - \beta_z^2 Z)/2$ . Analogously, energy levels  $\epsilon_{\mathcal{B},n}$  of  $H_{\mathcal{B}}$  are given by Eq. (C5) with  $\lambda' = \arccos(R'/\sqrt{Q'^2})$  instead of  $\lambda$ , where  $R' = (XYZ - \beta_x'^2 X - \beta_y'^2 Y - \beta_z'^2 Z)/2$ . In Eq. (C5), we label the energy levels with 1, 2, 3 instead of  $x, y, z$  corresponding to the zero-field eigenstates of Eq. (C4). For reasons of physical transparency, we continue to use the energies relabeled as  $\epsilon_{\mathcal{A},n} = \epsilon_{\mathcal{A},\mu}$ ,  $\epsilon_{\mathcal{B},m} = \epsilon_{\mathcal{B},\mu}$ , with  $\mu = x, y, z$ , without specifying the mappings  $n \rightarrow \mu$  and  $m \rightarrow \mu$  explicitly.

The simulation of the experimental MEL response suggests insignificant triplet-triplet dipolar and exchange coupling. Hence, we adopt the approximation of vanishing triplet-triplet interaction and represent the triplet-pair energy levels (i.e., the levels of the Hamiltonian  $H_{\mathcal{A}} + H_{\mathcal{B}}$ ) in terms of the sums of the two triplet energies

$$E_{\mu,\nu} = \epsilon_{\mathcal{A},\mu} + \epsilon_{\mathcal{B},\nu}, \quad \mu, \nu = x, y, z. \quad (\text{C6})$$

Thus, the field-dependent triplet-pair energy levels can be readily found, for arbitrary triplet-triplet and field orientations.

The analysis of triplet-pair energy levels shows that, at small triplet-triplet tilt angles and small angles between the magnetic field and the triplet  $z$  axis, some of the initially isolated levels, described by Eq. (C6), cross each other. As an example, we plot triplet-pair energy levels as a function of magnetic field in Fig. 9, for the relative triplet-tilt Euler angles ( $0.02\pi, 0.03\pi, 0.04\pi$ ), the azimuthal angle of the magnetic field of  $0.3\pi$ , and four different polar angles of the magnetic field, using the triplet ZFS parameters of the d-MEH-PPV MEL simulations in Fig. 5. The lower panels in Fig. 9 show the corresponding field-dependent triplet fusion rates,  $\delta\Phi$  in Eq. (11), i.e., the TTA components of the MEL, plotted with the simulation parameters of the d-MEH-PPV 50  $\mu\text{A}$  MEL curve shown in Fig. 5(b). In three out of the four geometric configurations in Fig. 9, a level crossing occurs in the energy spectrum, clearly reflected as a dip in the triplet fusion rate. In the fourth configuration, there is no level crossing, and the change of the triplet fusion rate with magnetic field appears less structured. This case represents the general picture seen throughout our simulations, in which the TTA component of the MEL consists of a smooth ‘‘hump’’ feature without any finer structure, corresponding to the case where the energy spectrum does not undergo a level crossing.

Figure 9 demonstrates that, in the absence of a level-crossing resonance, the triplet fine structure is *not* reflected in the MEL signal. However, it is difficult to draw any final conclusions regarding the shape of the MEL response

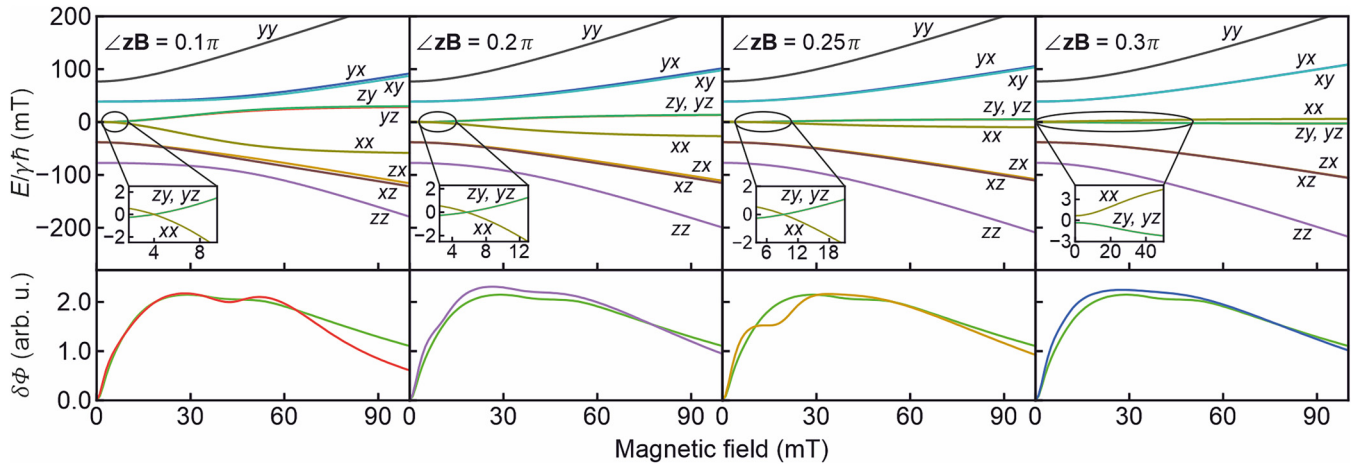


FIG. 9. Calculated magnetic-field dependence of the energy levels of a pair of triplet excitons (upper panels), using  $D = 58$  mT and  $E = 19$  mT and fixed triplet-triplet tilt Euler angles  $(\phi, \theta, \psi) = (0.02\pi, 0.03\pi, 0.04\pi)$ , for four different angles between the  $z$  axis of one of the triplet excitons and the applied magnetic field. Triplet-pair levels are labeled in accordance with the pair-energy subscripts in Eq. (C6). The insets show a close-up of the level-crossing regions. Field-dependent triplet fusion rates for the corresponding configurations [ $\delta\Phi$  in Eq. (11)] are plotted in the lower panels, using the model parameters to describe the 50  $\mu$ A d-MEH-PPV MEL data shown in Fig. 5(b). The green lines in the lower panels show the triplet fusion rate of the model simulations in Fig. 5(b).

from the triplet-pair spectra alone as the latter are defined for fixed magnetic field and triplet directions, while the MEL response comes from a wide distribution of field and triplet orientations.

To visualize a more conclusive picture, we explored the field evolution of level crossings for a distribution of magnetic-field and triplet orientations and evaluated the respective configuration-space volumes (recall that we work in the coordinate frame of triplet  $\mathcal{A}$ , so the magnetic field points in an arbitrary direction). After some simple reformulation, we determine the condition for level crossings as

$$\frac{\beta_x^2 + \beta_x'^2}{2\beta^2}X + \frac{\beta_y^2 + \beta_y'^2}{2\beta^2}Y + \frac{\beta_z^2 + \beta_z'^2}{2\beta^2}Z = \frac{XYZ}{\beta^2}. \quad (\text{C7})$$

In Eq. (C7), the left-hand side is a function of the orientation of the field and of the Euler angles  $(\phi, \theta, \psi)$ , but not of the field strength, whereas the right-hand side is a function of the field strength and does not depend on its orientation. We therefore plot the probability density function (PDF) of values on the left-hand side of Eq. (C7) next to the hyperbola representing the right-hand side of Eq. (C7) in Fig. 10.

One can expect a well-resolved triplet fine structure in the MEL signal if the positions of level crossings coincide for a number of configurations of the magnetic-field and triplet orientations. These level-crossing positions, as well as the relative multiplicity of coinciding positions in the configuration space, can be determined from Fig. 10. In particular, from Fig. 10(a) it is seen that the relative multiplicity of configurations with constrained triplet-triplet tilt angles exceeds that of the powder-averaged configurations in the domain of the largest absolute values (i.e., the shaded domains up to the dashed lines, between approximately  $-39$  and  $-20$  mT). At the same time, this is the domain of the steepest descent of the line in Fig. 10(b), where the level-crossing positions are closely packed. In contrast, in the remaining domain of solutions (shaded areas above the dashed lines,

from  $-20$  to  $0$  mT), the level-crossing positions are widely dispersed. It can therefore be expected that the effect of level-crossing resonances is averaged out within this domain, while their occurrence rates are higher among the

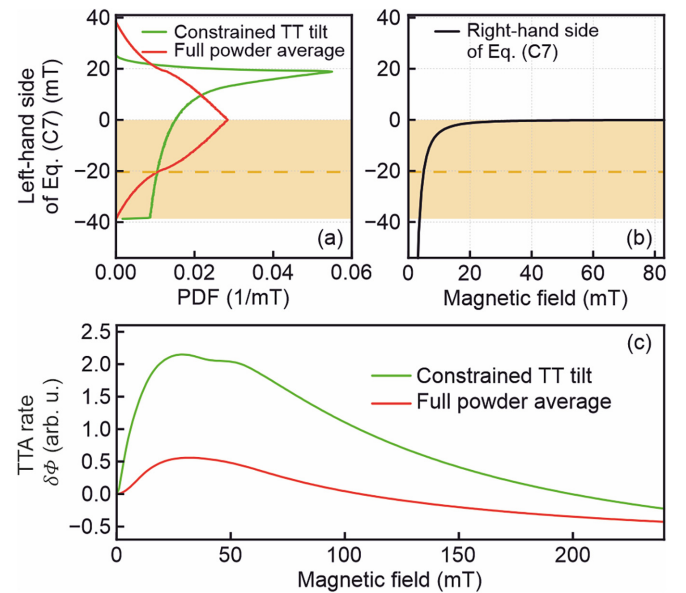


FIG. 10. The two probability distribution functions (PDFs) of the left-hand side of Eq. (C7), for the case where the triplet-triplet tilt angle is constrained by a maximal angle of  $\vartheta = 10^\circ$  (green) and for the full powder average (red), are plotted in panel (a) next to the right-hand side of Eq. (C7) in panel (b), using the simulation parameters of the d-MEH-PPV MEL in Fig. 5. Shaded areas indicate the domain where Eq. (C7) has a solution. Dashed lines mark the value at which the relative weight of the configurations with constrained triplet-triplet tilt angles surpasses the relative weight of the powder-averaged configurations. (c) Calculated triplet fusion rates corresponding to the green and red PDFs in (a). The green line is the same as that in Fig. 9.

powder-averaged configurations, as follows from Fig. 10(a). These observations explain the existence of the shallow dip in the triplet fusion rate for the constrained triplet-triplet tilt angles in Fig. 10(c), while such a feature is not seen in the fusion rate for the powder-averaged ensemble.

We speculate that the dependence of the triplet fusion rate on the tilt angle and the resulting emergence of the triplet fine structure in TTA-induced MEL is of a more general validity and will be relevant to other amorphous systems with disordered orientations of triplet excitations.

- 
- [1] S. Jamali, V. V. Mkhitarian, H. Malissa, A. Nahlawi, H. Popli, T. Grünbaum, S. Bange, S. Milster, D. M. Stoltzfus, A. E. Leung, T. A. Darwish, P. L. Burn, J. M. Lupton, and C. Boehme, Floquet spin states in OLEDs, *Nat. Commun.* **12**, 465 (2021).
- [2] T. Grünbaum, S. Milster, H. Kraus, W. Ratzke, S. Kurrmann, V. Zeller, S. Bange, C. Boehme, and J. M. Lupton, OLEDs as models for bird magnetoception: Detecting electron spin resonance in geomagnetic fields, *Farad. Discuss.* **221**, 92 (2020).
- [3] T. Grünbaum, V. V. Mkhitarian, E. Schmid, F. Dallinger, S. Bange, W. Jiang, T. A. Darwish, P. L. Burn, and J. M. Lupton, Highly anisotropic magnetoresistance of organic light-emitting diodes at geomagnetic field strengths, *Phys. Rev. B* **108**, 035201 (2023).
- [4] P. J. Hore and H. Mouritsen, The radical-pair mechanism of magnetoreception, *Annu. Rev. Biophys.* **45**, 299 (2016).
- [5] U. E. Steiner and T. Ulrich, Magnetic-field effects in chemical-kinetics and related phenomena, *Chem. Rev.* **89**, 51 (1989).
- [6] A. J. Schellekens, W. Wagemans, S. P. Kersten, P. A. Bobbert, and B. Koopmans, Microscopic modeling of magnetic-field effects on charge transport in organic semiconductors, *Phys. Rev. B* **84**, 075204 (2011).
- [7] V. N. Prigodin, J. D. Bergeson, D. M. Lincoln, and A. J. Epstein, Anomalous room temperature magnetoresistance in organic semiconductors, *Synth. Met.* **156**, 757 (2006).
- [8] T. Scharff, W. Ratzke, J. Zipfel, P. Klemm, S. Bange, and J. M. Lupton, Complete polarization of electronic spins in OLEDs, *Nat. Commun.* **12**, 2071 (2021).
- [9] J. Wang, A. Chepelianskii, F. Gao, and N. C. Greenham, Control of exciton spin statistics through spin polarization in organic optoelectronic devices, *Nat. Commun.* **3**, 1191 (2012).
- [10] R. C. Johnson and R. E. Merrifield, Effects of magnetic fields on the mutual annihilation of triplet excitons in anthracene crystals, *Phys. Rev. B* **1**, 896 (1970).
- [11] R. E. Merrifield, Magnetic effects on triplet exciton interactions, *Pure Appl. Chem.* **27**, 481 (1971).
- [12] V. Ern and R. E. Merrifield, Magnetic field effect on triplet exciton quenching in organic crystals, *Phys. Rev. Lett.* **21**, 609 (1968).
- [13] F. Braun, T. Scharff, T. Grünbaum, E. Schmid, S. Bange, V. V. Mkhitarian, and J. M. Lupton, Polaron-induced upconversion from triplets to singlets: Fluorescence- and phosphorescence-resolved optically detected magnetic resonance of OLEDs, *Phys. Rev. Appl.* **20**, 044076 (2023).
- [14] A. Obolda, Q. M. Peng, C. Y. He, T. Zhang, J. J. Ren, H. W. Ma, Z. G. Shuai, and F. Li, Triplet-polaron-interaction-induced upconversion from triplet to singlet: A possible way to obtain highly efficient OLEDs, *Adv. Mater.* **28**, 4740 (2016).
- [15] D. M. Stoltzfus, G. Joshi, H. Popli, S. Jamali, M. Kavand, S. Milster, T. Grünbaum, S. Bange, A. Nahlawi, M. Y. Teferi, S. I. Atwood, A. E. Leung, T. A. Darwish, H. Malissa, P. L. Burn, J. M. Lupton, and C. Boehme, Perdeuteration of poly[2-methoxy-5-(2'-ethylhexyloxy)-1,4-phenylenevinylene] (d-MEH-PPV): Control of microscopic charge-carrier spin-spin coupling and of magnetic-field effects in optoelectronic devices, *J. Mater. Chem. C* **8**, 2764 (2020).
- [16] X. Wei, B. C. Hess, Z. V. Vardeny, and F. Wudl, Studies of photoexcited states in polyacetylene and poly(paraphenylenevinylene) by absorption detected magnetic-resonance: The case of neutral photoexcitations, *Phys. Rev. Lett.* **68**, 666 (1992).
- [17] T. D. Nguyen, G. Hukic-Markosian, F. Wang, L. Wojcik, X.-G. Li, E. Ehrenfreund, and Z. V. Vardeny, Isotope effect in spin response of  $\pi$ -conjugated polymer films and devices, *Nat. Mater.* **9**, 345 (2010).
- [18] R. C. Roundy and M. E. Raikh, Slow dynamics of spin pairs in a random hyperfine field: Role of inequivalence of electrons and holes in organic magnetoresistance, *Phys. Rev. B* **87**, 195206 (2013).
- [19] S. P. Kersten, A. J. Schellekens, B. Koopmans, and P. A. Bobbert, Magnetic-field dependence of the electroluminescence of organic light-emitting diodes: A competition between exciton formation and spin mixing, *Phys. Rev. Lett.* **106**, 197402 (2011).
- [20] T. D. Nguyen, B. R. Gautam, E. Ehrenfreund, and Z. V. Vardeny, Magnetoconductance response in unipolar and bipolar organic diodes at ultrasmall fields, *Phys. Rev. Lett.* **105**, 166804 (2010).
- [21] W. J. Baker, D. R. McCamey, K. J. van Schooten, J. M. Lupton, and C. Boehme, Differentiation between polaron-pair and triplet-exciton polaron spin-dependent mechanisms in organic light-emitting diodes by coherent spin beating, *Phys. Rev. B* **84**, 165205 (2011).
- [22] M. Pope and C. E. Swenberg, *Electronic Processes in Organic Crystals and Polymers* (Oxford University Press, Oxford, UK, 1999).
- [23] Y. F. Wang, K. Sahin-Tiras, N. J. Harmon, M. Wohlgenannt, and M. E. Flatté, Immense magnetic response of exciplex light emission due to correlated spin-charge dynamics, *Phys. Rev. X* **6**, 011011 (2016).
- [24] H. Malissa, R. Miller, D. L. Baird, S. Jamali, G. Joshi, M. Bursch, S. Grimme, J. van Tol, J. M. Lupton, and C. Boehme, Revealing weak spin-orbit coupling effects on charge carriers in a  $\pi$ -conjugated polymer, *Phys. Rev. B* **97**, 161201 (2018).
- [25] G. Joshi, M. Y. Teferi, R. Miller, S. Jamali, D. Baird, J. van Tol, H. Malissa, J. M. Lupton, and C. Boehme, Isotropic effective spin-orbit coupling in a conjugated polymer, *J. Am. Chem. Soc.* **140**, 6758 (2018).
- [26] P. Desai, P. Shakya, T. Kreouzis, W. P. Gillin, N. A. Morley, and M. R. J. Gibbs, Magnetoresistance and efficiency measurements of Alq<sub>3</sub>-based OLEDs, *Phys. Rev. B* **75**, 094423 (2007).
- [27] W. J. Baker, T. L. Keevers, J. M. Lupton, D. R. McCamey, and C. Boehme, Slow hopping and spin dephasing of

- coulombically bound polaron pairs in an organic semiconductor at room temperature, *Phys. Rev. Lett.* **108**, 267601 (2012).
- [28] G. Joshi, R. Miller, L. Ogden, M. Kavand, S. Jamali, K. Ambal, S. Venkatesh, D. Schurig, H. Malissa, J. M. Lupton, and C. Boehme, Separating hyperfine from spin-orbit interactions in organic semiconductors by multi-octave magnetic resonance using coplanar waveguide microresonators, *Appl. Phys. Lett.* **109**, 103303 (2016).
- [29] U. Albrecht and H. Bässler, Langevin-type charge carrier recombination in a disordered hopping system, *Phys. Status Solidi B* **191**, 455 (1995).
- [30] F. L. Liu, H. van Eersel, P. A. Bobbert, and R. Coehoorn, Three-dimensional modeling of bipolar charge-carrier transport and recombination in disordered organic semiconductor devices at low voltages, *Phys. Rev. Appl.* **10**, 054007 (2018).
- [31] Y. Q. Jiang, H. Geng, W. Shi, Q. Peng, X. Y. Zheng, and Z. G. Shuai, Theoretical prediction of isotope effects on charge transport in organic semiconductors, *J. Phys. Chem.* **5**, 2267 (2014).
- [32] J. Partee, E. L. Frankevich, B. Uhlhorn, J. Shinar, Y. Ding, and T. J. Barton, Delayed fluorescence and triplet-triplet annihilation in  $\pi$ -conjugated polymers, *Phys. Rev. Lett.* **82**, 3673 (1999).
- [33] S. L. Bayliss, A. D. Chepelianskii, A. Sepe, B. J. Walker, B. Ehrler, M. J. Bruzek, J. E. Anthony, and N. C. Greenham, Geminate and nongeminate recombination of triplet excitons formed by singlet fission, *Phys. Rev. Lett.* **112**, 238701 (2014).
- [34] S. Engmann, E. G. Bittle, L. J. Richter, R. K. Hallani, J. E. Anthony, and D. J. Gundlach, The role of orientation in the MEL response of OLEDs, *J. Mater. Chem. C* **9**, 10052 (2021).
- [35] M. Reufer, M. J. Walter, P. G. Lagoudakis, B. Hummel, J. S. Kolb, H. G. Roskos, U. Scherf, and J. M. Lupton, Spin-conserving carrier recombination in conjugated polymers, *Nat. Mater.* **4**, 340 (2005).
- [36] J. E. Lawrence, A. M. Lewis, D. E. Manolopoulos, and P. J. Hore, Magnetoelectroluminescence in organic light-emitting diodes, *J. Chem. Phys.* **144**, 214109 (2016).
- [37] T. H. Tennahewa, S. Hosseinzadeh, S. I. Atwood, H. Popli, H. Malissa, J. M. Lupton, and C. Boehme, Coherent and incoherent spin-relaxation dynamics of electron-hole pairs in a  $\pi$ -conjugated polymer at low magnetic fields, *Phys. Rev. B* **109**, 075303 (2024).
- [38] K. J. van Schooten, D. L. Baird, M. E. Limes, J. M. Lupton, and C. Boehme, Probing long-range carrier-pair spin-spin interactions in a conjugated polymer by detuning of electrically detected spin beating, *Nat. Commun.* **6**, 6688 (2015).
- [39] V. V. Mkhitaryan, D. Danilović, C. Hippola, M. E. Raikh, and J. Shinar, Comparative analysis of magnetic resonance in the polaron pair recombination and the triplet exciton-polaron quenching models, *Phys. Rev. B* **97**, 035402 (2018).
- [40] L. D. Landau and E. M. Lifshitz, *Quantum Mechanics* (Pergamon, New York, 1965).